CrystEngComm

PAPER

View Article Online
View Journal | View Issue

Cite this: *CrystEngComm*, 2026, **28**, 419

Exploration of two highly fluorinated ammonium cations as spacers in low- and mixed dimensional hybrid lead iodide perovskites†

Concetta Bafaro, [a] Sofia Girolmoni, [a] Cesare Boriosi, [ab] Edoardo Mosconi, [b] Marco Cavazzini, [b] Simonetta Orlandi, [b] Francesco Toniolo, [c] Giulia Grancini, [c] Mohammad Khaja Nazeeruddin, [d] Ferdinando Costantino *[a] and Gianluca Pozzi *[b]

Received 15th September 2025,
Accepted 1st December 2025

DOI: 10.1039/d5ce00894h

rsc.li/crystengcomm

We here report the synthesis of 2D perovskites based on highly fluorinated organic cations (**LF8** and **SMS28**) that impart high hydrophobicity and thermal stability to the resulting materials. Stability tests showed that 2D perovskites $(\mathbf{SMS28})_2PbI_4$ and $(\mathbf{LF8})_2PbI_4$ maintained their structural properties unchanged for over a month of exposure to 75% relative humidity (RH), demonstrating high resistance to severe environmental conditions. When applied as top layers on films of a typical 3D perovskite ($MAPbI_3$) employed in photovoltaic cells, these fluorinated 2D materials slowed down the structural deterioration processes triggered by water infiltration as compared to unprotected samples, even at high RH conditions. The results highlight the potential of these coatings as a hydrophobic barrier to increase the environmental stability of common 3D perovskites, offering the possibility of improving the long-term protection of moisture-sensitive materials.

Introduction

Hybrid lead halide perovskites of the general formula AMX_3 (A = small organic ammonium cation, M = Pb^{2+}, X = halogen anion) characterized by a three dimensional (3D) structure were firstly used as photoactive materials in solar cells in 2009.[1] Since then, the field of perovskite photovoltaics has seen impressive scientific and technological advancements, with the highest-performing laboratory-scale single-junction perovskite solar cell reaching a certified power conversion efficiency (PCE) value of 27.0%.[2] Significant progress towards the future industrialization of perovskite photovoltaics has been also achieved, with successful demonstration of prototype modules and panels.[3,4] However, the reduced stability of perovskite based devices under operative conditions still represent a serious threat for the success of this technology.[5]

A range of strategies has been devised to solve stability issues.[6–9] In particular, the inherent sensitivity of archetypal 3D AMX_3 perovskites such $CH_3NH_3PbI_3$ ($MAPbI_3$) to ambient conditions has been targeted through compositional and dimensional engineering.[10–20] Thus, self-assembled low dimensional perovskites were introduced, where organic bilayers of suitable organic cations RNH_3^+ (or monolayers of α,ω-bisammonium cations) alternate with stacks of n layers of corner-sharing MX_6 octahedra.[13–15] These materials were synthesized by controlled mixing of solutions containing a RNH_3^+ salt (*e.g.* $PhCH_2CH_2NH_3I$) and the precursors of AMX_3 (*e.g.* PbI_2 and CH_3NH_3I). By varying the stoichiometric ratio of the starting components, materials of the general formula $(RNH_3)_2A_{n-1}M_nX_{3n+1}$ that are characterized by different n values could be obtained. For low dimensional perovskite with $n \leq 3$, high phase purity, excellent environmental and operational stability, and tuneable band gaps from 2.6 eV to 1.7 eV going from $n = 1$ to $n = 3$ were reported, but their direct use as photoactive layer led to average results in terms of PCE values as a consequence of their wide band gaps, low charge mobility, and high exciton binding energies.[13–15,20] Low dimensional perovskites with $n > 3$ were found to provide a better balance between the superior stability of 2D perovskites $(RNH_3)_2MX_4$ and the optimal optoelectronics parameters exhibited by 3D AMX_3 perovskites.[15,18] Thanks to their narrower band gaps, absorption edges down to 1.5 eV, and higher charge carrier mobility they have the potential for

[a] *Department of Chemistry, Biology and Biotechnologies, University of Perugia, 06123 Perugia, Italy. E-mail: ferdinando.costantino@unipg.it*
[b] *CNR Institute of Chemical Sciences and Technologies "Giulio Natta" (CNR-SCITEC), 20133 Milan, Italy. E-mail: gianluca.pozzi@scitec.cnr.it*
[c] *Department of Chemistry, University of Pavia, 27100 Pavia, Italy*
[d] *School of Integrated Circuits, Southeast University, Wuxi, Jiangsu, 214026 P. R. China*

† Dedicated to Professor Resnati, celebrating a career in fluorine and noncovalent chemistry on the occasion of his 70th birthday.

being successfully integrated into efficient perovskite solar cells. It was early recognized, however, that these materials, in particular those characterized by a theoretic n value >5 as determined by the stoichiometric ratio of the precursors, are actually constituted by a mixture of layered phases characterized by different n values, where AMX_3 co-exists.[21] Materials of this kind are sometimes referred to as quasi-3D perovskites.[19] In light of this, mixed dimensional perovskites for photovoltaic applications and beyond have been intentionally created using tailored RNH_3^+ cations acting as spacers between the stacks of inorganic layers.[18,19]

The same cations are instrumental for the creation of so called 2D/3D perovskite heterostructures, where a thin protective capping layer of 2D (or low dimensional) perovskite self-assembles on top of the bulk 3D AMX3 material.[16,22] In the practice, this is conveniently achieved by spin coating a solution containing the ammonium salt on top of the 3D perovskite layer, leading to the replacement of the A-site cations on the exposed AMX_3 surface with RNH_3^+.[23] Besides providing a barrier towards moisture, the 2D layer enhances the thermal- and photostability of the material due to the passivation of trap or defect states at the grain boundaries.

To date several aliphatic, arylic, and heterocyclic primary ammonium cations have been investigated as spacers in low dimensional and mixed dimensional perovskites.[19,24] Their structural diversity is a key-element for the design of materials with tuned stability and optoelectronic properties. In any case, these spacers must fulfil steric requirements for their correct interposition between inorganic sheets and for the occurrence of efficient hydrogen bonding interactions between the charged headgroup and halide ions in MX_6 octahedra, the major driving force for the self-assembly and stabilization of low dimensional perovskites.[25] The existence of additional non-covalent interactions that depend on the nature of the spacer can also play an important role, as evidenced by low dimensional or 2D/3D perovskites in which ω-haloalkylammonium- or *p*-halobenzylammonium cations are used as spacers to give rise to highly directional halogen bonds[26] that contribute to enhance the order and stability of the materials and to adjust their optoelectronic parameters.[27–29]

In this respect, the insertion of fluorine atoms in the backbone of the organic spacer broadens the range of opportunities by allowing further specific non-covalent interactions, among which C–F···H, F···F, C–F···π, that have been harnessed in crystal engineering and in the systematic design of functional materials.[30] This approach proved to be successful also in the development of low- and mixed dimensional perovskites for photovoltaic applications,[31] where the fluorination of spacer cations has been identified as an effective tool to improve the material characteristics and the efficiency and operational stability of the devices. Early studies were conducted using mono- or trifluorinated ethylammonium cations,[32,33] but the focus soon shifted to low- and mixed dimensional materials fabricated with cations featuring aryl units bearing from one to five fluorine atoms, in particular phenethylammonium derivatives.[34–37] Such cations are characterized by large dipole moments and can give rise to non-covalent interactions involving π effect. This leads to materials with lower exciton binding energies and increased interlayer charge mobilities,[38] that better fit the requirements for their integration in highly efficient solar cells.

We showed that some fully saturated organic ammonium cations featuring perfluoroalkyl molecular fragments C_nF_{2n+1} (n = 4 to 6, see Fig. 1) can be likewise used to form very stable 2D hybrid lead halide perovskites with an extremely strong hydrophobic character.[39–42] Here, fluorophobic interactions,[43] which are irrelevant in the case of cations with limited fluorination degree,[44] are central to the self-assembly process and to the solid-state structural arrangements. Using the branched cation **A43** as a model, it was demonstrated that during the one-step fabrication of low dimensional perovskites $(\mathbf{RNH_3})_2A_{n-1}M_nX_{3n+1}$ fluorophobic interactions facilitate the auto-segregation of low-dimensional perovskite phases on top of bulk 3D film, spontaneously affording photoactive 2D/3D materials without resorting to any special technique. Solar cells fabricated with such materials exhibited improved stability and >20% PCE.[39]

The size and shape of these organic cations were found to exert a deep influence on the optoelectronic properties of the corresponding 2D perovskites by inducing local distortions of the inorganic sheets, as clarified by DFT and *ab initio* calculations that also pointed toward smaller band gap and better charge transport properties for 2D materials based on elongated, linear cations such as **LF6**.[40] Furthermore, a deep photophysical and computational study provided compelling evidence for the existence of long-lived weakly bound charge pairs in the 2D perovskite $(\mathbf{A43})_2PbI_4$, due to combined structural effect and electrostatic effects due to the bulky $(CF_3)3C$-tail group that promote the formation of spatially confined hole states at the valence band edge and stabilize loosely interacting electron–hole pairs with reduced recombination and longer lifetimes.[42]

Our previous studies evidenced that the introduction of highly fluorinated ammonium cations as structural elements can provide 2D perovskites materials with intriguing physical

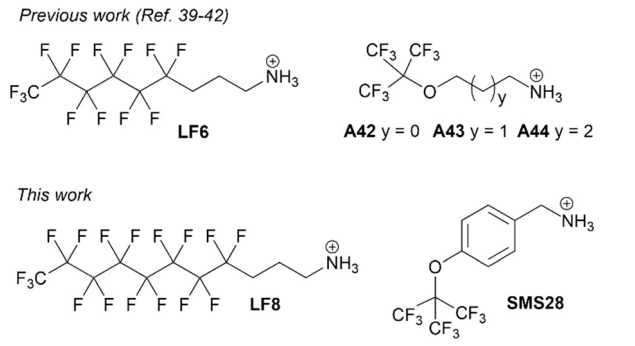

Fig. 1 Structures of linear and branched highly fluorinated cations.

characteristics, quite different from those observed in the case of their non-fluorinated (or less-fluorinated) analogues. They also revealed that even minimal structural modifications of these cations can deeply influence in an unexpected way various functional parameters of the final materials. However, their real scope in the hybrid perovskite field is yet to be determined, mostly because the very limited set of compounds made available so far. In the effort to fill this gap, we have now synthesized two new highly fluorinated cations, **LF8** and **SMS28** in the linear and branched series, respectively (Fig. 1), which have been investigated as possible components of low- and mixed dimensional hybrid lead iodide perovskites. **LF8** was designed to further push fluorophobic interactions while questioning the suggested effects of the chain elongation, whereas the aryl group in **SMS28** was introduced to take advantage of additional π interactions and larger dipole moment. Experimental data corroborated by computational studies demonstrated their incorporation into 2D lead halide perovskite materials. Furthermore, we found that the introduction of **SMS28** or **LF8** in the layered structure does not significantly alter the thermal and optical properties of the resulting 2D perovskite $(RNH_3)_2PbI_4$, except for a slight red-shift absorption which was found in the UV-visible analysis of $(\mathbf{SMS28})_2PbI_4$. Suitable $(RNH_3)_2PbI_4$ crystals for data collections were synthesized in the case of **SMS28** using a solvothermal treatment, followed by slow cooling of the reaction medium to room temperature. Quasi-3D perovskite thin films and 2D/3D bilayers were also fabricated and their stability under controlled humidity conditions was assessed. The aromatic cation **SMS28** has proven to be a more appropriate water-repellent capping agent on the surface of the $MAPbI_3$ compared to the heterojunction containing **LF8** on the top of the same 3D perovskite. Conversely, during the fabrication of 2D/3D hybrid perovskite by layer spin coating deposition, the presence of **LF8** was beneficial by preventing the formation of segregated 2D phases within the preformed $MAPbI_3$ structure.

Experimental

General

Dimethyl sulfoxide (DMSO, Alfa Aesar, ACS reagent ≥99.9%), dimethylformamide (DMF, Carlo Erba, RPE reagent), lead nitrate ($Pb(NO_3)_2$, Carlo Erba, RPE reagent 99.5%), potassium iodide (KI, Panreac, ACS reagent ≥99.5%), hydriodic acid (HI, Sigma Aldrich, 57% wt in H_2O, 99.95%), toluene (Carlo Erba, RPE reagent), diethyl ether (RPE reagent), and all commercially available solvents and reagents employed in the synthesis of the highly fluorinated ammonium salts were used as received.

X-ray Powders Diffraction (XRPD) patterns were acquired by a PANalytical X'PERT PRO instrument using a Cu Kα radiation (λ = 1.54187 Å) at a scan rate of 0.1422° s^{-1} and 2θ diffraction angle range from 20° to 70°. Single crystals data collection was carried out on a D8 Venture single crystal diffractometer with MoKα radiation at 150 °K using a Cryostream Oxford cooling system.

Materials indexing was performed using GSAS-II software. Experimental and simulated 3D material structures were visualized using VESTA. Thermal Gravimetric Analysis (TGA) and Differential Thermal Analysis (DTA) were performed using a Netzsch STA 449C analyser with a heating rate of 10 °C min^{-1} under an 80 mL min^{-1} and a 40 mL min^{-1} flux of N_2 and O_2, respectively. Thin films were fabricated with a WS-650 series spin processor. SEM images (Fig. S8–S11) were acquired using a FEG LEO 1525 Zeiss instrument. Dimensional measurements on the SEM and water contact angle images were performed using the Image-J software. Moisture resistance tests were performed on thin films exposed to either ambient air or stored in a desiccator containing a saturated aqueous NaCl solution to simulate a controlled 75% relative humidity (RH) chamber (see Fig. S7).[45] The structural integrity of the materials was monitored over time by XRPD analysis. After converting the transmittance data (Fig. S2) to absorbance values, the bandgap energy (E_g) was determined through a Tauc plot analysis. Using the general Tauc equation $(\alpha h\nu)^n = A(h\nu - E_g)$, the x-intercept in the plot represents the optical E_g. The n exponential was set at 2, since metal halide perovskites are classified as direct bandgap semiconductors.[46] In this case, $(\alpha h\nu)^2$ was plotted as a function of the energy expressed in eV, where ν is the frequency of the incident light source and h is the Planck's constant.

Synthesis of $RNH_3^+I^-$

The iodide salts of cation **LF8** and cation **SMS28** (**LF8**-I and **SMS28**-I, respectively) were obtained by addition of stoichiometric amounts of 57% aqueous HI to the corresponding amines 4,4,5,5,6,6,7,7,8,8,9,9,10,10,11,11,11-heptadecafluoroundecan-1-amine and 4-(nonafluoro-*tert*-butyloxy)benzylamine suspended in MeOH followed by evaporation of liquid phase. Detailed synthetic procedures and analytical data are reported in the SI.

$(RNH_3)_2PbI_4$ single crystals growth

Following a procedure reported for analogous materials,[39,40] $(\mathbf{SMS28})_2PbI_4$ crystals were obtained by mixing in an autoclave a stoichiometric amount of the organic in molar ratio 2 : 1 of the salt **SMS28**-I (0.4 mmol, 187.63 mg) and PbI_2 (0.2 mmol, 92.90 mg) in concentrated HI (6.0 mL) and then heating at 100 °C for 24 h. The autoclave was cooled to room temperature at a rate of 7 °C h^{-1} to promote the crystals growth. Very flat single crystals of $(\mathbf{SMS28})_2PbI_4$ were obtained.

The growth of $(\mathbf{LF8})_2PbI_4$ single crystals was also attempted in the same way but no suitable crystals for data collection were obtained.

$(RNH_3)_2PbI_4$ powders

2D perovskite powders were obtained by slow evaporation at 70 °C of 0.75 mL of a DMSO solution containing the fluorinated ammonium salt **LF8**-I or **SMS28**-I (1.15 M) and

PbI_2 (0.57 M) in a 2 : 1 molar ratio. The materials formation was confirmed by XRPD patterns (Fig. S3).

$(RNH_3)_2PbI_4$ thin films

Firstly, glass substrates were sequentially cleaned for 15 minutes in an ultrasonic bath using detergent, deionized water, ethanol and acetone. DMSO solutions containing the fluorinated ammonium salt and PbI_2 were prepared in concentrations of 1.15 M and 0.575 M, respectively. These solutions were deposited on glass by spin coating at 1000 rpm for 10 s and then at 5000 rpm for 30 s.[39,41] During this last spinning step, 100 μL of toluene were added to promote the crystallization and to improve the morphology and the uniformity of the film.[47] The resulting films were annealed at 100 °C for 15 minutes. In the case of (**SMS28**)$_2PbI_4$, the same spin-coating recipe was additionally applied for the deposition of a thin film from an ink containing the pre-formed (**SMS28**)$_2PbI_4$ powder (0.34 M in DMSO).

Quasi-3D perovskite thin films

To realize the quasi-3D perovskite thin film using $MAPbI_3$ as the bulk 3D component, the following spin coating procedure, based on a previous literature example,[39] was applied. A DMSO solution containing PbI_2 (1.15 M) and MAI (1.15 M) (solution A) and a DMSO solution containing the fluorinated salts **SMS28**-I or **LF8**-I (1.15 M) and PbI_2 (0.575 M) were prepared. Mother solutions A and B were mixed at room temperature in the following volume ratios:

1) 800 μL of A and 200 μL of B to obtain a molar ratio RNH_3^+ : PbI_2 = 20% mol in the mixture;

2) 900 μL of A and 100 μL of B to obtain a molar ratio RNH_3^+ : PbI_2 = 10% mol in the mixture;

3) 940 μL of A and 60 μL of B to obtain a molar ratio RNH_3^+ : PbI_2 = 6% mol in the mixture.

The resulting solutions (1–3) were sonicated for 5 minutes and spin coated on glass at 1000 rpm for 10 s (with an acceleration of 200 rpm s^{-1}) and then at 5000 rpm for 30 s (with an acceleration of 1000 rpm s^{-1}). During the last 10 s at 5000 rpm, 100 μL of toluene was added to promote the crystallization of the final material. A film annealing process was performed at 100 °C for 50 minutes.

2D/3D heterojunctions fabrication

Firstly, a 3D perovskite thin film ($MAPbI_3$) was deposited by spin-coating a solution containing equimolar amounts of PbI_2 and CH_3NH_3I in DMF/DMSO 9 : 1 v/v on glass (1000 rpm for 10 s and then at 5000 rpm for 45 s).[48] During the last 35 s at 5000 rpm, diethyl ether was added dropwise to favour the crystallization of $MAPbI_3$.[49] A film annealing process was carried out at 50 °C for 2 minutes and then at 100 °C for 10 minutes. For the 2D fluorinated capping layer on $MAPbI_3$, a fluorinated salt dispersion was prepared in a concentration of 6 mg mL^{-1} in isopropyl alcohol (IPA). The resulting dispersion was spin coated on top of the preformed $MAPbI_3$ film at 5000 rpm for 30 s and the resulting film was reheated at 100 °C for 5 min.[39]

Computational details

The first-principles calculations based on density functional theory (DFT) were carried out as implemented in the PWSCF Quantum-Espresso package.[50] Geometry optimization was performed using the Perdew–Burke–Ernzherof (PBE) functional,[51] and including DFT-D3 dispersion.[52] The electrons-ions interactions were described by norm-conserving pseudo-potentials with electrons from H 1s; C, N, O, F 2s, 2p; I 5s, 5p; Pb 6s, 6p, 5d; shells explicitly included in calculations.[53] A cutoff of 80Ry was used for the wavefunctions and a *k*-points sampling of 4 × 4 × 1.[54] The starter unit cell was the (**A43**)$_2PbI_4$,[42] where the cation was substituted and the *c*-axis was elongated accordingly.

Electronic band gap and DOS were calculated by single-point hybrid calculations including spin–orbit coupling (SOC) on the PBE-D3 geometry. These calculations were conducted using the hybrid HSE06 functional (α = 0.43) and DFT-D3 dispersion with norm-conserving full relativistic pseudo-potentials,[53] with electrons from H 1s; C, N, O, F 2s, 2p; I 5s, 5p; Pb 5s, 5p, 6s, 6p, 5d; shells explicitly included in calculations, with keeping the same *k*-point grid and wavefunctions cutoff and using a cutoff for the Fock grid of 80Ry.

To evaluate the passivation energy, DFT calculations were carried out on the (001) $MAPbI_3$ surface within the supercell approach by using the PBE functional and ultrasoft pseudopotentials (shells explicitly included in calculations: F 2s, 2p; Br 4s, 4p; I 5s, 5p; N, C 2s, 2p; H 1s; Pb 6s, 6p, 5d) and a cutoff on the wavefunctions of 40 Ryd (320 Ryd on the charge density). Slabs models were built starting from the tetragonal phase of $MAPbI_3$, by fixing cell parameters to the experimental values.[55] Vacuum (10 Å) was added along the non-periodic direction perpendicular to the slabs. Starting from the flat PbI_2-terminated (001) surface, a symmetric disposition of the organic cations on the external layers of the slabs was adopted leading to supercells with zero average dipole moments.

Passivation energies (E_{pass}) were calculated according to the equation:

$$E_{pass} = [E_{SMS28I\text{-}term} - (E_{bare} - 16 \times E_{SMS28I})]/16$$

where $E_{SMS28\text{-}term}$ is the total energy of the $MAPbI_3$ passivated system; E_{bare} is the energy of the PbI_2-terminated slab; E_{SMS28I} is the energy of the isolated **SMS28**-I salt. We normalized E_{pass} dividing by the number of molecules (16) which correspond to the number of the undercoordinated Pb atoms on the two surfaces.

Results and discussion

Characterization of materials

XRPD of $(RNH_3)_2PbI_4$ thin films. For both salts, XRPD patterns confirmed the formation of 2D materials by the

presence of reflections at <3.00° 2θ values, relating to interlayer distances of 31.29 Å and 24.00 Å for $(\mathbf{LF8})_2PbI_4$ and $(\mathbf{SMS28})_2PbI_4$, respectively (Fig. 2 and Table 1).

These angle values correspond to interlayer distances compatible with a double layer arrangement of the organic cation between the $[PbI_6]^{4-}$ octahedron motifs.

Based on precedent studies, the presence of pre-formed 2D perovskite seeds in the ink solution could preserve the "memory" of the dissolved crystals, thus promoting a fast nucleation and a controlled grains growth.[56] With the aim of bypassing the intermediate *n*-phase in the 2D perovskite, we have also prepared $(\mathbf{SMS28})_2PbI_4$ thin films dissolving $(\mathbf{SMS28})_2PbI_4$ powders in DMSO to obtain a dispersion for spin coating depositions. Compared to the film previously obtained with $(\mathbf{SMS28})_2PbI_4$ (Fig. 2b), a preferential orientation of the material towards the 001 plane (2θ = 3.68°) was observed in the XRPD pattern in Fig. S4.

TGA and DTA of $(RNH_3)_2PbI_4$ powders. Thermal analysis of $(RNH_3)_2PbI_4$ was performed on 2D perovskite powders (see Fig. S3 for XRPD patterns).

The thermo-gravimetric profiles (TGA, black lines in Fig. 3a and c) of both $(RNH_3)_2PbI_4$ showed a similar behaviour, with a first weight loss around 200 °C due to the sublimation of ammonium cations from the material. A further weight loss was observed around 400 °C, associated to the melting process of PbI_2. The thermal differential curves (DTA, red lines in Fig. 3a and c) do not highlight peaks at temperatures lower than 300 °C, commonly associated with phase transitions or deterioration processes in similar materials.[45,57] In the case of $(\mathbf{SMS28})_2PbI_4$ a first weight loss of 73% was observed between 200 °C and 400 °C (Fig. 3c). Based on the calculated molecular formula, we assumed to be associated with the sublimation of **SMS28** and I_2 from the material. An analogous behaviour was exhibited

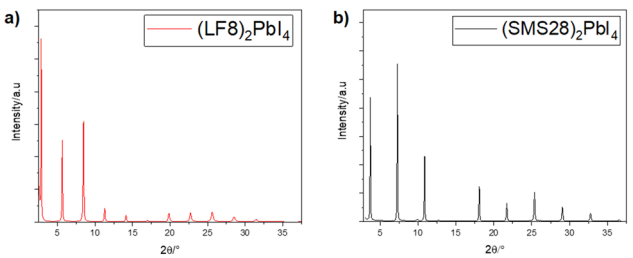

Fig. 2 XRPD patterns of a) $(\mathbf{LF8})_2PbI_4$ and b) $(\mathbf{SMS28})_2PbI_4$ thin films obtained by spin coating a solution of PbI_2 and RNH_3I in DMSO.

Table 1 *hkl* planes of $(RNH_3)_2PbI_4$ indexed from thin films diffraction patterns

	2θ (°)	*h k l*	Calculated *d* (Å)	Observed *d* (Å)
$(\mathbf{LF8})_2PbI_4$	2.82	0 0 1	31.33	31.29
	5.63	0 0 2	15.67	15.69
	8.45	0 0 3	10.44	10.46
$(\mathbf{SMS28})_2PbI_4$	3.68	0 0 1	24.57	24.00
	7.25	0 0 2	12.28	12.18
	10.84	0 0 3	8.19	8.15

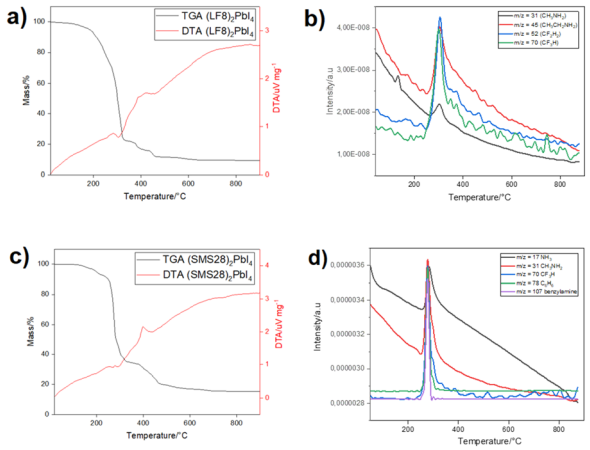

Fig. 3 a) TGA (black line) and DTA (red line) of $(\mathbf{LF8})_2PbI_4$ powder; b) MS analysis coupled with DTA for $(\mathbf{LF8})_2PbI_4$ powder; c) TGA (black line) and DTA (red line) of $(\mathbf{SMS28})_2PbI_4$ powder; d) and b) MS analysis coupled with DTA for $(\mathbf{SMS28})_2PbI_4$ powder.

by $(\mathbf{LF8})_2PbI_4$ in the same temperature range with a final weight loss of 77% (Fig. 3a). We coupled TGA measurements of 2D perovskites to mass spectrometry (MS) to evaluate which type of decomposition occurs in the temperature range 200–400 °C for the fluorinated cations **LF8** and **SMS28** (Fig. 3b and d, respectively). MS demonstrate that the first mass loss shown at 200 °C is associated for both 2D materials with a combination of fragmentation and volatilization of the organic ammonium cations rather than to simple sublimation. In particular, the released fragments of $(\mathbf{LF8})_2PbI_4$ (Fig. 3b) included *m*/*z* = 31 (CH_3NH_2), 45 ($CH_3CH_2NH_2$), 52 (CF_2H_2), and 70 (CF_3H), while the detected ions for $(\mathbf{SMS28})_2PbI_4$ (Fig. 3d) were *m*/*z* = 17 (NH_3), 31 (CH_3NH_2), 70 (CF_3H), 78 (C_6H_6), and 107 ($C_6H_5CH_2NH_2$). These fragments are consistent with cleavage of the N–C and C–F bonds of the organic spacers, supporting that the first decomposition event involves partial breakdown and volatilization of the organic component. At temperatures higher than 400 °C we assumed that the sample residue is PbI_2 for both the materials, since the remaining mass was estimated to be about 461 g mol^{-1}. In fact, a further materials weight loss begins to be observed at about 400 °C, *i.e.* near the melting point of PbI_2 (403 °C). Both materials continue to lose mass even above 1000 °C, *i.e.* the boiling point of PbI_2 which is at 954 °C.

Single crystals and structural computational simulations. Very flat $(\mathbf{SMS28})_2PbI_4$ crystals with appreciable size were obtained for single crystal X-ray data collections. However, due to the lack of growth in the third dimension, only the measurement of the unit cell was performed together with the arrangement of the inorganic PbI_4^- layers, as shown in Fig. S5. No appreciable electron density was found along the *c*-axis, making the complete structure determination impossible.

Theoretical calculations were performed to complete the 2D material structure. Fig. 4a and S6a show the three-dimensional structure of the 2D perovskite $(\mathbf{SMS28})_2PbI_4$ obtained through DFT geometric optimization. This DFT

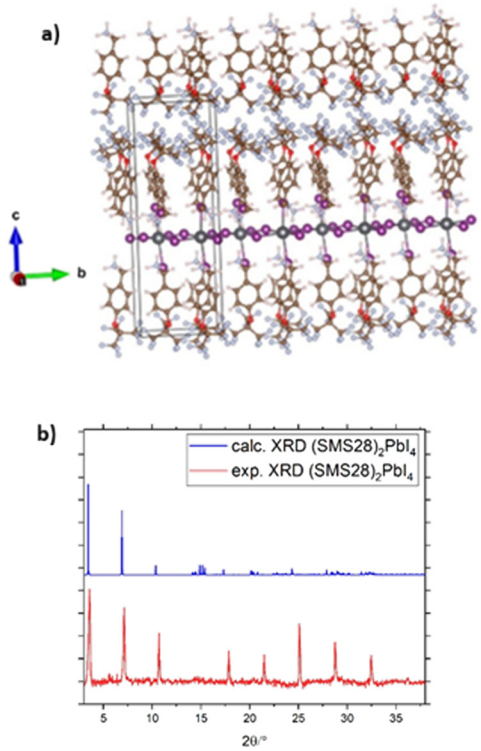

Fig. 4 a) Theoretical crystalline structure obtained from DFT geometrical optimization of $(\mathbf{SMS28})_2PbI_4$, view along the "a" axis; b) DFT simulated and experimental XRPD patterns of $(\mathbf{SMS28})_2PbI_4$ crystal powders.

optimized model was not used for the refinement of X-ray data due to lack of observed data along the *c*-axis. However, as reported in Fig. 4b, a comparison between the experimental and theoretical XRPD patterns of $(\mathbf{SMS28})_2PbI_4$ was carried out to verify the correspondence between the predicted 2D perovskite structure and the experimentally obtained material.

The main diffraction peaks observed experimentally coincide with those predicted by the theoretical model, confirming the formation of a Ruddlesden–Popper $n = 1$ phase consistent with the hypothesized layered structure for $(\mathbf{SMS28})_2PbI_4$ and supporting the validity of the proposed structural model. However, there are some additional weak reflections in the diffraction pattern predicted by the theoretical model (in the range 14–35° 2θ in Fig. 4b). This discrepancy can be attributed to the fact that DFT calculations assume an ideal, perfectly ordered structure, while the real sample could exhibit defects and stacking disorder typical of 2D materials, which could attenuate or eliminate the visibility of some reflections. The lattice parameters extracted from the experimental diffraction pattern fit are in good agreement with those calculated theoretically, supporting the structural assignment of $(\mathbf{SMS28})_2PbI_4$.

The experimental cell parameters obtained from the as-synthesized crystals, compared with the predicted structural cell, are summarized In Table 2.

Table 2 Experimental and theoretical cell parameters of $(\mathbf{SMS28})_2PbI_4$ crystals

	Experimental	Theoretical
Cell length (Å)	a = 8.639	a = 8.791
	b = 8.750	b = 8.823
	c = 24.674	c = 26.130
Cell angles (°)	α = 85.886	α = 89.650
	β = 86.272	β = 78.250
	γ = 88.962	γ = 88.810
Space group	$P\bar{1}$	$P1$
Volume (Å^3)	1856.2	1983.82

It is worth noting that single crystals could not be obtained in the case of LF8, possibly due to the high degree of molecular crystal disorder typical of compounds featuring medium-sized perfluoalkyl chains.[30]

$(RNH_3)_2PbI_4$ band gaps determination. The transmittance UV-vis spectra of the 2D perovskite thin films (Fig. S2) were manipulated as described in the Experimental section in order to extrapolate band gap (E_g) values from their respective Tauc plots, according to a common, although not strictly accurate practice followed for this kind of materials (Fig. 5).[58]

$(\mathbf{LF8})_2PbI_4$ and $(\mathbf{SMS28})_2PbI_4$ present similar estimated E_g values of about 2.65 eV. In both absorption spectra an intense peak appears at 2.4–2.6 eV, followed by a continuum absorption edge. These features are respectively related to excitonic and direct band-to-band transitions.[40] $(\mathbf{SMS28})_2PbI_4$ shows an excitonic signal centred at 2.45 eV, slightly red-shifted respect to the case of $(\mathbf{LF8})_2PbI_4$. Based on the optimized geometry, we further investigated the electronic properties by DFT density of states analysis (DOS, see Fig. S6c), obtaining a calculated band gap of 2.5 eV in good agreement with the experimental measurements. As shown in Fig. S6c, for $(\mathbf{SMS28})_2PbI_4$ DOS analysis reveals that the VBM is mainly characterized by the contribution of iodide and the CBM by lead, while the electronic contribution of the organic moiety is deep inside the bands with a slight coupling in the VB region appearing around from −0.7 eV.

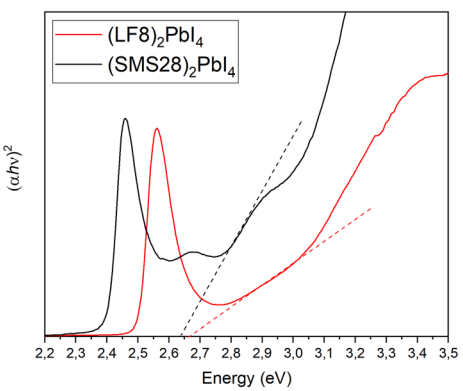

Fig. 5 $(RNH_3)_2PbI_4$ Tauc plot and corresponding extrapolated band gap values.

Moisture resistance tests

2D perovskites. The XRPD patterns of $(\mathbf{LF8})_2PbI_4$ and $(\mathbf{SMS28})_2PbI_4$ thin films, collected time by time, showed no variation after one month of exposure to ambient air or at 75% RH conditions (Fig. 6). This result supports the beneficial effect of the fluorinated groups in the bulky aliphatic/aromatic cation on the material resistance to drastic humidity conditions, in line with the expected higher hydrophobicity induced by fluorination.[36,59]

To evaluate the morphological stability of 2D perovskite films under demanding humid conditions, SEM images were acquired for $(\mathbf{LF8})_2PbI_4$ and $(\mathbf{SMS28})_2PbI_4$ films before and after one month exposure to 75% RH. As shown in Fig. S8a and b, S9a and b, the surface of both films maintained a homogeneous and compact morphology with no signs of degradation. SEM cross-sectional images (Fig. S8c and d, S9c and d) of the 2D perovskites $(\mathbf{LF8})_2PbI_4$ and $(\mathbf{SMS28})_2PbI_4$ were integrated to assess eventual degradation processes in the bulk of the films. After one month of exposure to RH 75%, the average thickness of both films was approximately 15 μm and remained essentially unchanged compared to freshly prepared samples. Furthermore, no signs of delamination or voids were observed in the cross sections. These results confirmed the morphological robustness and structural integrity of the **LF8**- or **SMS28**-based 2D perovskites upon prolonged exposure to humidity.

2D/3D heterojunction. Given the excellent results achieved by both the $(RNH_3)_2PbI_4$ materials against moisture degradation, we were interested in studying the effect of fluorinated cation following the fabrication of 2D/3D composites, aiming to create a water-repellent covering fluorinated layer on the top of the 3D perovskite bulk. The XRPD patterns of the resulting 2D/3D heterojunction materials containing **LF8** or **SMS28** as hydrophobic capping layers on the top of 3D $MAPbI_3$ perovskite are reported in Fig. 7.

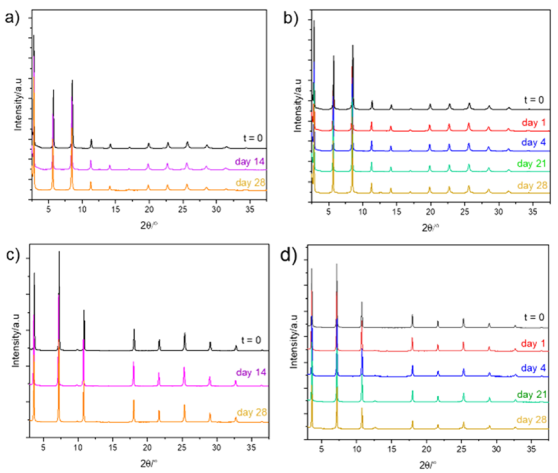

Fig. 6 $(LF8)_2PbI_4$ relative humidity tests a) in ambient air and b) at RH 75%. $(SMS28)_2PbI_4$ relative humidity tests c) in ambient air and d) at RH 75%.

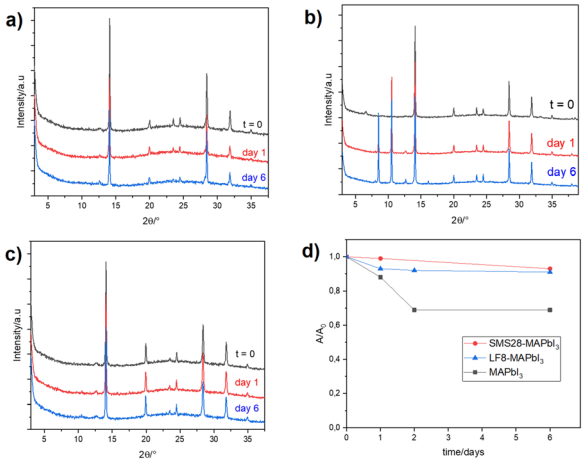

Fig. 7 Humidity resistance test (RH75%) of a) $MAPbI_3$, b) **LF8**-I/$MAPbI_3$, c) **SMS28**-I/$MAPbI_3$ thin films and d) degradation kinetics of the $MAPbI_3$ layer over time.

While the composite **SMS28**/$MAPbI_3$ did not show any significant structural changes after 6 days from the start of the test (Fig. 7c), alterations could be seen in the XRPD pattern of the composite **LF8**/$MAPbI_3$ (Fig. 7b). Indeed, after one day exposure to RH 75%, the appearance of reflections localized at 8–11° typical of $MAPbI_3$ hydrated phases could be observed for the **LF8**/$MAPbI_3$ heterojunction. In any case, for both 2D/3D materials, the presence of the 2D layer was found to reduce the degradation rate of the underlying 3D perovskite, as shown by comparing the degradation curves of films of pure and capped $MAPbI_3$ that were obtained through the evaluation of the decrease in intensity of the 3D perovskite reflection at 14° over time (Fig. 7d).

Planar SEM images of the **LF8**/$MAPbI_3$ and **SMS28**/$MAPbI_3$ heterojunctions (Fig. S10a and S11a) showed that the 2D **LF8**- or **SMS28** based capping layer formed a continuous and compact covering on the $MAPbI_3$ surface. After 5 days of exposure to RH 75%, the morphology of the **LF8** or **SMS28**-based heterojunctions did not undergo significant degradation processes (Fig. S10b and S11b). Conversely, a series of voids and irregularities appeared on the unprotected surface of the perovskite $MAPbI_3$ due to the drastic humidity conditions (Fig. S12b). Cross-sectional SEM images (Fig. S10c and S11c) confirmed the formation of a well-defined bilayer structure. The 2D capping layer is clearly distinguishable as a thin, conformal layer on the $MAPbI_3$ surface, indicating good interfacial contact. The absence of voids or discontinuities at the interface highlights the effective encapsulation of the underlying perovskite, which is responsible for the improved moisture resistance and long-term stability. The thickness of the 2D **LF8**- or **SMS28**-based capping layer on the $MAPbI_3$ surface is approximately 6.0 μm in both cases, which remains almost unchanged even after 5 days of exposure to RH 75% (Fig. S10d and S11d).

The capability of **SMS28** and **LF8** in the protection and passivation of the 3D perovskite was next computationally investigated by simulating the interface between $MAPbI_3$ and

an interacting cation passivating layer (see Fig. S6c and Computational details). Following a procedure previously reported,[60,61] we were able to calculate a spontaneous passivation energy (E_{pass}) of −2.4 and −2.6 eV per molecule for **SMS28** and **LF8**, respectively, that indicates a strong interaction with the perovskite surface even higher than that calculated for a recently developed, highly efficient passivating agent such as dimethylphenethylsulfonium iodide,[61] thus supporting the stability found experimentally.

Water contact angle measurements. Static water contact angle measurements were performed for 2D perovskite films based on **LF8** and **SMS28** cations, to evaluate the surface hydrophobicity before and after one month of exposure to RH 75%. As reported in Fig. S13, the freshly fabricated 2D perovskite films based on **LF8** and **SMS28** exhibit a contact angle of 96.5° and 84.9°, respectively. This data confirmed the superior surface hydrophobicity of the saturated **LF8** cation, compared to the aromatic **SMS28**. This result can be explained by the fact that the presence of long alkyl chains in (**LF8**)$_2$PbI$_4$ imparts a higher water repellent character than the (**SMS28**)$_2$PbI$_4$ material containing a more polar cation. Furthermore, the linear arrangement of alkyl chains in (**LF8**)$_2$PbI$_4$, compared to the assembly of bulky cations in (**SMS28**)$_2$PbI$_4$, could contribute to the formation of a more compact hydrophobic barrier. The hydrophobic character of 2D perovskite films was slightly reduced after one month of exposure to RH 75%: the contact angle of the **LF8**-based material decreased to 88.9°, while for the **SMS28**-based film it decreased to 77.4°. We were also interested in evaluating the effect of a fluorinated 2D-perovskite capping layer on the MAPbI$_3$ surface, so static water contact angle measurements were performed on as prepared MAPbI$_3$ films that were found to exhibit a contact angle of about 73° (Fig. S14e), indicating a relatively high degree of wettability. After the spin-coating deposition of **SMS28**-I or **LF8**-I on the MAPbI$_3$ surface and the generation of the corresponding 2D-perovksite capping layer, the water contact angle respectively increases to 90.6° and 116.9° (Fig. S14a and c). These results confirmed the increased surface hydrophobicity of the 2D/3D heterojunction due to the presence of fluorinated organic groups on the surface of the structure. After 5 days of exposure to RH 75%, the contact angle of the fluorinated capped heterojunctions remained almost unchanged (from 90.6° to 89.8° in the case of **SMS28**/MAPbI$_3$, Fig. S14d) or underwent a slight decrease in hydrophobicity (from 116.9° to 107.5° in the case of **LF8**/MAPbI$_3$, Fig. S14b). Conversely, the MAPbI$_3$ contact angle decreased significantly from 72.9° to 57.8°, due to a significant humidity-induced surface degradation (Fig. S14f). These results clearly demonstrate that **LF8**- or **SMS28**-based fluorinated 2D perovskite capping effectively protects the underlying MAPbI$_3$ layer and preserves its hydrophobic character over time.

"**Quasi 3D**" **perovskites.** We finally evaluated the effect of the addition of the new highly fluorinated cations to the precursors of MAPbI$_3$ on the formation of "quasi 3D"materials with different fluorination degrees. The XRPD pattern of the "quasi-3D" hybrid perovskites thus obtained are reported in Fig. 8.

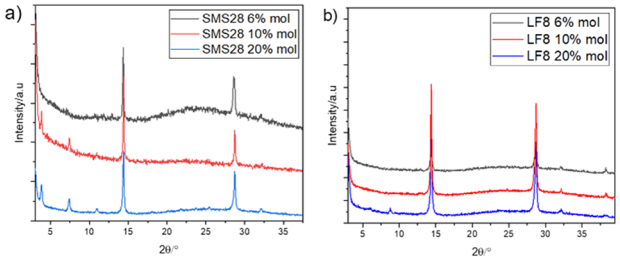

Fig. 8 XRPD pattern of "quasi-3D" hybrid perovskites containing a) **SMS28** and b) **LF8** at different molar ratios.

Interestingly, the appearance of typical 2D-perovskite reflections at $2\theta < 10°$, in addition to the characteristic reflections of the pure MAPbI$_3$, was observed in the XRPD pattern of the hybrid "quasi-3D" perovskite MAPbI$_3$–**SMS28** even at low **SMS28** : PbI$_2$ molar ratio (10% mol). This feature is possibly related to segregation of a low dimensional phase in the bulk, as already observed in similar materials based on organic ammonium cations containing phenyl groups.[53,62] Indeed, this phenomenon was much less evident in the case of the hybrid material MAPbI3–**LF8**, where minor 2D-perovskite reflections could be observed only at **SMS28** : PbI$_2$ = 20% mol.

From the XRPD patterns reported in Fig. S15 and S16, both hybrid materials undergo a severe degradation process. In particular, the **LF8**–MAPbI$_3$ hybrid material was drastically altered by humidity after only one day of testing. We hypothesized that this aspect could be related to the presence of structural defects between the 3D perovskite domains and those of the 2D component of the composite, probably due to a poor interaction between the fluorinated cation and the polar structure of the MAPbI$_3$ lattice. Other factors that we believe may favor the infiltration of water into the composite, could be related to crystallographic interruptions caused by the sterically bulky cations **LF8** and **SMS28** at the grain boundaries and to a non-homogeneous distribution of the cations in the composite.

This aspect was not further explored in the present work, as the preliminary results obtained were not sufficiently satisfactory to warrant a detailed discussion.

Conclusions

In this work, we developed and characterized novel 2D materials based on highly fluorinated cations (**LF8** and **SMS28**) capable of withstanding critical environmental conditions, demonstrating good resistance up to approximately 200 °C and maintaining their structural integrity even after a month of exposure to 75% relative humidity. Applied as a protective capping layers on 3D perovskite films (MAPbI$_3$), these fluorinated materials demonstrated an effective barrier action, significantly slowing the degradation processes typically triggered by the presence

of humidity. These results highlight the potential of hydrophobic and functional coatings to increase the environmental stability of 3D perovskites, without resorting to direct modifications of their chemical composition. Future studies will assess how adding these protective layers to photovoltaic heterojunctions affects their stability and long-term performance. This approach may contribute to the development of more robust and reliable perovskite technologies suitable for use in real life situations, even beyond the photovoltaic field.[63,64]

Author contributions

F. C., G. P. Conceptualization, supervision, funding acquisition, writing – original draft. Co. B., S. G. Data curation and formal analysis. Ce. B., E. M., M. C., S. O., F. T. Investigation, writing – review & editing. G. C., M. K. N. Methodology.

Conflicts of interest

There are no conflicts to declare.

Data availability

The data supporting this article have been included as part of the supplementary information (SI). Supplementary information: synthesis details, characterization of new compounds and materials, DFT simulations, SEM images, static water contact angle measurements. See DOI: https://doi.org/10.1039/d5ce00894h.

Acknowledgements

This work was possible thanks to the support of the International Activity "Laboratori congiunti tematici del CNR: Scienze Chimiche e Tecnologie dei Materiali (2025-2027), Designer molecules and materials for highly efficient, long lasting perovskite solar cells".

Notes and references

1 A. Kojima, K. Teshima, Y. Shirai and T. Miyasaka, *J. Am. Chem. Soc.*, 2009, **131**, 6050.
2 https://www.nrel.gov/pv/cell-efficiency.html (accessed July 12, 2025).
3 S. Pescetelli, A. Agresti, G. Viskadouros, S. Razza, K. Rogdakis, I. Kalogerakis, E. Spiliarotis, E. Leonardi, P. Mariani, L. Sorbello, M. Pierro, C. Cornaro, S. Bellani, L. Najafi, B. Martín-García, A. E. Del Rio Castillo, R. Oropesa-Nuñez, M. Prato, S. Maranghi, M. L. Parisi, A. Sinicropi, R. Basosi, F. Bonaccorso, E. Kymakis and A. Di Carlo, *Nat. Energy*, 2022, **7**, 597.
4 P. Zhu, C. Chen, J. Dai, Y. Zhang, R. Mao, S. Chen, J. Huang and J. Zhu, *Adv. Mater.*, 2024, **36**, 2307357.
5 H. Chen, L. Chu and W. Yan, *Adv. Funct. Mater.*, 2025, **35**, 2412389.
6 W. J. Jang, P. J. Park, J. Ma and S. Y. Kim, *Chem. Commun.*, 2025, **61**, 8137.
7 X. Xiong, Y. Yang, C. Zhu, H. Zhang, L. Zhang and X. Guo, *Coord. Chem. Rev.*, 2025, **532**, 216499.
8 J. Suo, B. Yang, D. Bogachuk, G. Boschloo and A. Hagfeldt, *Adv. Energy Mater.*, 2025, **15**, 2400205.
9 L. Mu, S. Wang, H. Liu, W. Li, L. Zhu, H. Wang and H. Chen, *Adv. Funct. Mater.*, 2025, **35**, 2415353.
10 M. Saliba, T. Matsui, J.-Y. Seo, K. J.-P. Correa-Baena, M. K. Nazeeruddin, S. M. Zakeeruddin, W. Tress, A. Abate, A. Hagfeldt and M. Grätzel, *Energy Environ. Sci.*, 2016, **9**, 1989.
11 Z. Wang, Z. Shi, T. Li, Y. Chen and W. Huang, *Angew. Chem., Int. Ed.*, 2017, **56**, 1190.
12 Ha. Lu, A. Krishna, S. M. Zakeeruddin, M. Grätzel and A. Hagfeldt, *iScience*, 2020, **23**, 101359.
13 I. C. Smith, E. T. Hoke, D. Solis-Ibarra, M. D. McGehee and H. I. Karunadasa, *Angew. Chem., Int. Ed.*, 2014, **53**, 11232.
14 D. H. Cao, C. C. Stoumpos, O. K. Farha, J. T. Hupp and M. G. Kanatzidis, *J. Am. Chem. Soc.*, 2015, **137**, 7843.
15 L. N. Quan, M. Yuan, R. Comin, O. Voznyy, E. M. Beauregard, S. Hoogland, A. Buin, A. R. Kirmani, K. I. Zhao, A. Amassian, D. H. Kim and E. H. Sargent, *J. Am. Chem. Soc.*, 2016, **138**, 2649.
16 G. Grancini, C. Roldán-Carmona, I. Zimmermann, E. Mosconi, X. Lee, D. Martineau, S. Narbey, F. Oswald, E. De Angelis, M. Grätzel and M. K. Nazeeruddin, *Nat. Commun.*, 2017, **8**, 15684.
17 J. Zhang, D. Bai, Z. Jin, H. Bian, K. Wang, J. Sun, Q. Wang and S. Liu, *Adv. Energy Mater.*, 2018, **8**, 1703246.
18 G. Grancini and M. K. Nazeeruddin, *Nat. Rev. Mater.*, 2019, **4**, 4.
19 T. L. Leung, I. Ahmad, A. A. Syed, A. Man Ching Ng, J. Popović and A. B. Djurišić, *Commun. Mater.*, 2022, **3**, 63.
20 S. Teale, M. Degani, B. Chen, E. H. Sargent and G. Grancini, *Nat. Energy*, 2024, **9**, 779.
21 R. Quintero-Bermudez, A. Gold-Parker, A. H. Proppe, R. Munir, Z. Yang, S. O. Kelley, A. Amassian, M. F. Toney and E. H. Sargent, *Nat. Mater.*, 2018, **17**, 900.
22 Z. Wang, Q. Lin, F. P. Chmiel, N. Sakai, L. M. Herz and H. J. Snaith, *Nat. Energy*, 2017, **2**, 17135.
23 K. T. Cho, G. Grancini, Y. Lee, E. Oveisi, J. Ryu, O. Almora, M. Tschumi, P. A. Schouwink, G. Seo, S. Heo, J. Park, J. Jang, S. Paek, G. Garcia-Belmonte and M. K. Nazeeruddin, *Energy Environ. Sci.*, 2018, **11**, 952.
24 H. B. Lee, N. Kumar, B. Tyagi, S. He, R. Sahani and J.-W. Kang, *Mater. Today Energy*, 2021, **21**, 100759.
25 H. Pan, X. Zhao, X. Gong, Y. Shen and M. Wang, *J. Phys. Chem. Lett.*, 2019, **10**(8), 1813.
26 G. Cavallo, P. Metrangolo, R. Milani, T. Pilati, A. Priimagi, G. Resnati and G. Terraneo, *Chem. Rev.*, 2016, **116**, 2478.
27 S. Sourisseau, N. Louvain, W. Bi, N. Mercier, D. Rondeau, F. Boucher, J.-Y. Buzare and C. Legein, *Chem. Mater.*, 2007, **19**, 600.
28 M.-H. Tremblay, J. Bacsa, B. Zhao, F. Pulvirenti, S. Barlow and S. R. Marder, *Chem. Mater.*, 2019, **31**, 6145.
29 X. Fu, T. He, S. Zhang, X. Lei, Y. Jiang, D. Wang, P. Sun, D. Zhao, H.-Y. Hsu, X. Li, M. Wang and M. Yuan, *Chem*, 2021, **7**, 3131.

30 R. Berger, G. Resnati, P. Metrangolo, E. Weber and J. Hulliger, *Chem. Soc. Rev.*, 2011, **40**, 3496.
31 G. Mohanty, A. Sebastian, S. Haritha, K. N. Parida and I. Neogi, *J. Mater. Chem. C*, 2022, **10**, 16949.
32 C. Lermer, S. T. Birkhold, I. L. Moudrakovski, P. Mayer, L. M. Schoop, L. Schmidt-Mende and B. V. Lotsch, *Chem. Mater.*, 2016, **28**, 6560.
33 D. Bi, P. Gao, R. Scopelliti, E. Oveisi, J. Luo, M. Grätzel, A. Hagfeldt and M. K. Nazeeruddin, *Adv. Mater.*, 2016, **28**, 2910.
34 J. Hu, I. W. H. Oswald, S. J. Stuard, M. M. Nahid, N. Zhou, O. F. Williams, Z. Guo, L. Yan, H. Hu, Z. Chen, X. Xiao, Y. Lin, Z. Yang, J. Huang, A. M. Moran, H. Ade, J. R. Neilson and W. You, *Nat. Commun.*, 2019, **10**, 1276.
35 J. Hu, I. W. H. Oswald, H. Hu, S. J. Stuard, M. M. Nahid, L. Yan, Z. Chen, H. Ade, J. R. Neilson and W. You, *ACS Mater. Lett.*, 2019, **1**, 171.
36 F. Zhang, D. H. Kim, H. Lu, J.-S. Park, B. W. Larson, J. Hu, L. Gao, C. Xiao, O. G. Reid, X. Chen, Q. Zhao, P. F. Ndione, J. J. Berry, W. You, A. Walsh, M. C. Beard and K. Zhu, *J. Am. Chem. Soc.*, 2019, **141**, 5972.
37 J. Shi, Y. Gao, X. Gao, Y. Zhang, J. Zhang, X. Jing and M. Shao, *Adv. Mater.*, 2019, **31**, 1901673.
38 L. Yan, C. J. Gloor, A. M. Moran and W. Youa, *Appl. Phys. Lett.*, 2023, **122**, 240501.
39 K. T. Cho, Y. Zhang, S. Orlandi, M. Cavazzini, I. Zimmermann, A. Lesch, N. Tabet, G. Pozzi, G. Grancini and M. K. Nazeeruddin, *Nano Lett.*, 2018, **18**, 5467.
40 I. García-Benito, C. Quarti, V. I. E. Queloz, S. Orlandi, I. Zimmermann, M. Cavazzini, A. Lesch, S. Marras, D. Beljonne, G. Pozzi, M. K. Nazeeruddin and G. Grancini, *Chem. Mater.*, 2018, **30**, 8211.
41 I. García-Benito, C. Quarti, V. I. E. Queloz, Y. J. Hofstetter, D. Becker-Koch, P. Caprioglio, D. Neher, S. Orlandi, M. Cavazzini, G. Pozzi, J. Even, M. K. Nazeeruddin, Y. Vaynzof and G. Grancini, *Front. Chem.*, 2020, **7**, 946.
42 V. I. E. Queloz, M. E. F. Bouduban, I. García-Benito, A. Fedorovskiy, S. Orlandi, M. Cavazzini, G. Pozzi, H. Trivedi, D. C. Lupascu, D. C. Beljonne, J. Moser, M. K. Nazeeruddin, C. Quarti and G. Grancini, *Adv. Funct. Mater.*, 2020, 202000228.
43 G. Cavallo, A. Abate, M. Rosati, G. P. Venuti, T. Pilati, G. Terraneo, G. Resnati and P. Metrangolo, *ChemPlusChem*, 2021, **86**, 469.
44 M. Zhang, T. Larison, S. Tu, O. Kuksenok and M. Stefik, *ACS Appl. Polym. Mater.*, 2022, **4**, 7042.
45 N. Vanni, D. Morelli Venturi, E. Radicchi, G. Quaglia, E. Cambiotti, L. Latterini, F. De Angelis and F. Costantino, *Adv. Mater. Interfaces*, 2021, **8**, 2101888.
46 K. Kranthiraja, S. Aryal, M. Temsal, M. Sharma and A. B. Kaul, *Solar*, 2022, **2**, 385.
47 M. Xiao, F. Huang, W. Huang, Y. Dkhissi, Y. Zhu, J. Etheridge, A. Gray-Weale, U. Bach, Y. Cheng and L. Spiccia, *Angew. Chem., Int. Ed.*, 2014, **53**, 9898.
48 Y. Shang, W. Meng, F. Lu, H. Li, Z. Yuan and N. Li, *Adv. Mater.*, 2025, 2504602.
49 N. Ahn, D.-Y. Son, I.-H. Jang, S. M. Kang, M. Choi and N.-G. Park, *J. Am. Chem. Soc.*, 2015, **137**, 8696.
50 P. Giannozzi, S. Baroni, N. Bonini, M. Calandra, R. Car, C. Cavazzoni, D. Ceresoli, G. L. Chiarotti, M. Cococcioni, I. Dabo, A. Dal Corso, S. de Gironcoli, S. Fabris, G. Fratesi, R. Gebauer, U. Gerstmann, C. Gougoussis, A. Kokalj, M. Lazzeri, L. Martin-Samos, N. Marzari, F. Mauri, R. Mazzarello, S. Paolini, A. Pasquarello, L. Paulatto, C. Sbraccia, S. Scandolo, G. Sclauzero, A. P. Seitsonen, A. Smogunov, P. Umari and R. M. Wentzcovitch, *J. Phys.: Condens. Matter*, 2009, **21**, 395502.
51 J. P. Perdew, K. Burke and M. Ernzerhof, *Phys. Rev. Lett.*, 1996, **77**, 3865.
52 S. Grimme, J. Antony, S. Ehrlich and H. Krieg, *J. Chem. Phys.*, 2010, **132**, 154104.
53 M. J. van Setten, M. Giantomassi, E. Bousquet, M. J. Verstraete, D. R. Hamann, X. Gonze and G.-M. Rignanese, *Comput. Phys. Commun.*, 2018, **226**, 39.
54 H. J. Monkhorst and J. D. Pack, *Phys. Rev. B: Solid State*, 1976, **13**, 5188.
55 A. Poglitsch and D. Weber, *J. Chem. Phys.*, 1987, **87**, 6373.
56 S. Sidhik, W. Li, M. H. K. Samani, H. Zhang, Y. Wang, J. Hoffman, A. K. Fehr, M. S. Wong, C. Katan, J. Even, A. B. Marciel, M. G. Kanatzidis, J. Blancon and A. D. Mohite, *Adv. Mater.*, 2021, **33**, 2007176.
57 N. Yantara, F. Yanan, C. Shi, H. A. Dewi, P. P. Boix, S. G. Mhaisalkar and N. Mathews, *Chem. Mater.*, 2015, **27**, 2309.
58 S. Zhao, B. Zhao, Y. Chen, G. Yang and X. Li, *ACS Appl. Energy Mater.*, 2019, **2**, 6230.
59 H. Hong, S. Guo, L. Jin, Y. Mao, Y. Chen, J. Gu, S. Chen, X. Huang, Y. Guan, X. Li, Y. Li, X. Lu and Y. Fu, *Nat. Commun.*, 2024, **15**, 3164.
60 B. Yang, J. Suo, E. Mosconi, D. Ricciarelli, W. Tress, F. De Angelis, H.-S. Kim and A. Hagfeldt, *ACS Energy Lett.*, 2020, **5**, 3159.
61 J. Suo, B. Yang, E. Mosconi, D. Bogachuk, T. A. S. Doherty, K. Frohna, D. J. Kubicki, F. Fu, Y. Kim, O. Er-Raji, T. Zhang, L. Baldinelli, L. Wagner, A. N. Tiwari, F. Gao, A. Hinsch, S. D. Stranks, F. De Angelis and A. Hagfeldt, *Nat. Energy*, 2024, **9**, 172.
62 S. J. Yang, K. Wang, Y. Luo, J. Y. Park, H. Yang, A. H. Coffey, K. Ma, J. Sun, S. Wieghold, C. Zhu and L. Dou, *ACS Energy Lett.*, 2023, **8**, 3693.
63 S. Aftab, Z. Ali, M. Imtiaz Hussain, M. A. Assiri, N. Rubab, F. Ozel and E. Akman, *Carbon Energy*, 2025, **7**, e70018.
64 C. Liang, H. Gu, J. Xia, T. Liu, S. Mei, N. Zhang, Y. Chen and G. Xing, *Carbon Energy*, 2023, **5**, e251.

